batteries

MDPI

Article

An Empirical Multi-Stage One-Step Battery Thermal Runaway Model Based on Arrhenius Reaction Rate Formalism

Alexander Ruth *, Martin Hantinger, Alexander Machold and Andreas Ennemoser

AVL List GmbH, Hans-List-Platz 1, 8020 Graz, Austria; martin.hantinger@avl.com (M.H.); alexander.machold@avl.com (A.M.); andreas.ennemoser@avl.com (A.E.)
* Correspondence: alexander.ruth@avl.com; Tel.: +43-(03)-167874441

Abstract

This study develops a multi-stage, Arrhenius-type reaction rate model for exothermic heat release during thermal runaway (TR) that depends on the local active material temperature, T_{Cell}, and the remaining reactant fraction, Y. Model parameters are identified from an accelerating rate calorimetry (ARC) test on an NMC721 pouch cell. Validation across other cell formats (cylindric and prismatic) and cathode chemistries (LCO, LMO, NCA, LFP) is left for future work. Model performance is evaluated in a 3D CFD (AVL FIRE™ M 2021.2) representation of the ARC assembly and benchmarked against Gaussian and polynomial one-step TR formulations that depend solely on T_{Cell}. The three TR models are further applied to a generic 4S4P pouch cell module under stagnant and actively cooled conditions to assess thermal propagation. In the ARC test, the Arrhenius-type model shows improved agreement with measured cell skin temperatures for the NMC721 cell; in the 4S4P module, it exhibits a trend toward higher thermal propagation rates relative to the Gaussian and polynomial models.

Keywords: battery; lithium-ion battery; abuse simulations; CFD; battery thermal runaway; battery hazard

Academic Editors: Xuan Zhou and Rongheng Li

Received: 7 August 2025
Revised: 25 September 2025
Accepted: 26 September 2025
Published: 9 October 2025

Citation: Ruth, A.; Hantinger, M.; Machold, A.; Ennemoser, A. An Empirical Multi-Stage One-Step Battery Thermal Runaway Model Based on Arrhenius Reaction Rate Formalism. *Batteries* **2025**, *11*, 371. https://doi.org/10.3390/batteries11100371

1. Introduction

Thermal runaway (TR) is the rapid self-heating of a battery cell caused by exothermic reactions within the cell's active materials, resulting in the release of the cell's stored chemical energy. It is commonly triggered by internal or external abuse conditions (e.g., short circuit, overcharge, mechanical deformation, or overheating due to cooling system failure or excessive internal resistance). This article focuses on thermally induced runaway caused by external overheating.

As discussed by Warner [1] and Pfrang et al. [2], Liu et al. [3], Citarella et al. [4], Ostanek et al. [5], and Menz [6], Li-ion battery thermal runaway follows a broadly consistent sequence. At elevated temperatures (~75–120 °C), decomposition of the SEI and reactions between lithium and the electrolyte generate flammable gases [1–3]. Around 130–150 °C (a commonly reported temperature range for onset to TR), polyolefin shutdown separators soften or melt, enabling pore closure and direct anode–cathode contact that can cause internal short circuits (ISC) and additional Joule heating [1–3]. Ceramic separators generally remain intact to higher temperatures [2]. Above ~150 °C, cathode–electrolyte reactions can become self-sustaining, releasing additional heat and sometimes oxygen [1–3]; peak cell temperatures of ~600–800 °C have been reported [4]. Gas build-up may lead to venting or rupture, and the flammable carbonate electrolyte poses a fire and explosion hazard [1–3].

Based on the temperature regimes discussed above, prior studies (e.g., Ostanek et al. [5] and Citarella et al. [4]) divide TR into stages based on single-cell ARC experiments, a framework adopted here to develop a multi-stage, one-step Arrhenius-type model. While model validation is performed for an NMC721 pouch cell in this study, similar stage-wise trends have been reported by Golubkov et al. [7] across LCO, NCA, and LFP chemistries, suggesting phenomenological transferability.

Beyond Li-ion, analogous safety concerns arise for emerging Na-ion batteries considered for stationary storage owing to their low cost and resource abundance. Li et al. [8] indicate that Na-ion cells can undergo thermal runaway via SEI/electrolyte decomposition, gas release, and exothermic cathode reactions, yet often show higher onset temperatures and lower exothermicity for certain chemistries (e.g., $NaCrO_2$ > 350 °C), suggesting greater intrinsic thermal robustness than Li-ion. These observations imply that stage-wise kinetic models, like our multi-stage one-step Arrhenius framework, could be transferable to Na-ion; however, this is not demonstrated here and remains future work.

While the multi-stage, one-step framework is generic, the reaction parameters for Li-ion batteries are not. The literature shows that TR behavior systematically depends on SoC and SoH (Han et al. [9], Garcia et al. [10], Willstrand et al. [11], Essl et al. [12], Bugryniec et al. [13], Golubkov et al. [14], and Pfrang et al. [2]), with lower SoC/SoH shifting the onset to higher temperatures and reducing severity and heat release. Consequently, the model's predictive capability depends on prior parameter identification from experiments, and TR model parameters must be identified for the specific cell under study.

Beyond the battery operating state, cell format also affects the parameters inferred from ARC. Essl et al. [15] report lower T_{onset} and T_{max} for prismatic hard case cells versus pouch cells of otherwise similar design. Thus, hard case formats, such as cylindrical and prismatic cells, may require format-specific calibration to identify the multi-stage reaction rate model parameters and to correct systematic bias in surface temperature measurements introduced by the hard case's thermal resistance. In this study, we, therefore, use a thin-laminate NMC721 pouch cell and validate the TR model against single-cell ARC data, allowing us to evaluate model quality rather than format effects and to perform a direct comparison with common one-step formulations (Gaussian, polynomial).

Improving Li-ion battery safety requires reducing the probability and severity of initiating faults and enhancing heat dissipation to delay the transition to self-sustaining reactions. In engineering studies, these questions are typically addressed with 3D CFD conjugate heat transfer (CHT) thermal propagation (TP) analyses. To evaluate the TR model performance and enable a one-to-one comparison with common one-step formulations (Gaussian, polynomial), we simulate a generic 4S4P pouch cell module in 3D CFD under stagnant and actively cooled conditions.

2. Thermal Runaway Model

2.1. Gaussian Thermal Runaway Model

As proposed by Yeow et al. [16], one option to model TR in Li-ion batteries is a Gaussian distribution for the exothermal heat release depending on the battery cell temperature as measured, for example, in an ARC test. Such an empirical replication of the heat release is adopted here from Citarella et al. [4], hereafter named the Gaussian model.

The TR model of Citarella et al. [4] builds on two sub-models. The first part of the model refers to stage 2 of TR according to Ostanek et al. [5]. Stage 2 uses an exponential ansatz assuming quasi-adiabatic conditions. It describes the initial SEI degradation, the initial exothermic reaction between intercalated lithium and electrolyte solvent, and the damage of the separator between anode and cathode.

The first part of the Citarella et al. [4] model turns active when the local active material temperature, $T_{Cell,i}(t)$, is $T_{onset,1} < T_{Cell,i}(t) < T_{onset,2}$. Both $T_{onset,1}$ and $T_{onset,2}$ are extracted from the ARC test, as indicated in Figure 1. The exothermal heat release, $\dot{q}_{Cell,i}(t)$, for the first part of their model is given by Citarella et al. [4] as follows:

$$\dot{q}_{Cell,i}(t) = A \cdot \exp\left(-\frac{E_a}{R_u T_{Cell,i}}\right) \cdot \frac{c_p \cdot m \cdot \Delta T}{Vol_{Cell}} \tag{1}$$

where $\Delta T = T_{onset,2} - T_{onset,1}$, R_u is the universal gas constant, E_a is the activation energy, A is the pre-exponential factor, c_p is the heat capacity of the battery cell, m is the mass of the battery cell, and Vol_{Cell} is the total volume of the battery cell.

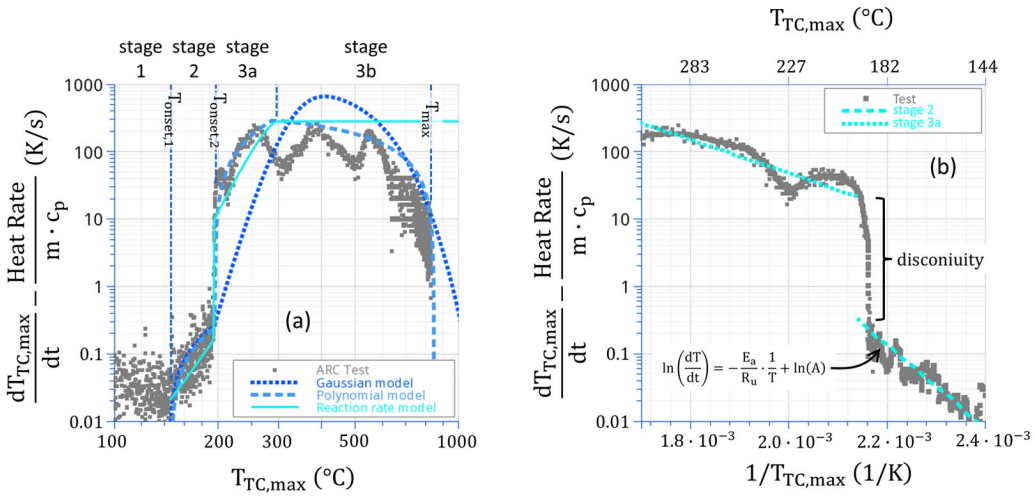

Figure 1. Accelerating rate calorimetry (ARC) results for the NMC721 pouch cell used in this study, as shown in Section 3: (**a**) measured cell skin temperature rate, dT/dt, overlaid with the Gaussian, polynomial, and reaction rate TR models, (**b**) identification of the reaction rate parameters for stage 2 and 3a of the reaction rate TR model according to Equations (19) and (20).

The second part of the Citarella et al. [4] model, which is stage 3 according to Ostanek et al. [5], describes the exothermal reaction of the cathode materials with the electrolyte and the heat due to ISC (Joule effect). This sub-model has a skew Gaussian form, and it becomes relevant as soon as $T_{Cell,i}(t) > T_{onset,2}$ as follows:

$$\dot{q}_{Cell,i}(t) = \frac{P_{factor}}{\sigma \cdot \sqrt{2 \cdot \pi}} \cdot \exp\left[-\frac{1}{2}\left(\frac{T_{Cell,i} - \mu}{\sigma}\right)^2\right] \cdot \left(1 + \mathrm{erf}\left[skew\left(\frac{T_{Cell,i} - \mu}{\sigma \cdot \sqrt{2}}\right)\right]\right) \tag{2}$$

where P_{factor} is a proportionality factor, σ is the standard deviation, and μ is the average value of the Gaussian. The parameters of Equations (1) and (2) are determined via correlation with ARC test data of the battery. An example of a heat release curve according to Citarella et al. [4] is given in Figure 1a.

$\dot{q}_{Cell,i}(t)$ is typically transferred as tabled data to the solver. The CFD software linearly interpolates between the given values, depending on local battery cell temperature, $T_{Cell,i}(t)$.

The exothermal heat release, $\dot{q}_{Cell,i}(t)$, is limited by the available total thermal energy, Q_{Cell}, inside the battery active material, as shown in Section 2.4. Here, $Q(t = 0) = Q_{Cell}$, which reduces during the progress of TR to zero according to the following:

$$\frac{\partial Q(t)}{\partial t} = -\dot{q}_{Cell,i}(t) \tag{3}$$

Polygon Resampling

An alternative to Citarella et al. [4] is a polygonal fit to the temperature rates of the ARC test according to Equations (14) and (15). From experience, the maximum envelope of the cell skin temperatures recorded in the test gives a good approximation of the test data for a CFD model as follows:

$$\dot{q}_{Cell,i}(t) = \frac{dT_{TC,max}}{dt} \cdot c_p \cdot m \tag{4}$$

where c_p is the heat capacity of the battery cell and m is the mass of the battery cell. The model is plotted along with ARC test data in Figure 1a. Hereafter, the model is named the "polynomial model".

2.2. Reaction Rate Thermal Runaway Model

Hatchard et al. [17] are one of the first to present an Arrhenius rate approach to model the heat release from the SEI, cathode, and anode during battery thermal runaway. Here, these active materials are considered as blends of components, like lithium, manganese, carbon, etc., which are made by Kim et al. [18], who later extended Hatchard's [17] model by including the electrolyte decomposition at elevated temperatures >200 °C. Coman et al. [19] adopted Hatchard's [17] model and extended it by the heat contribution from the electrochemical reaction due to ISC. Each of these publications uses cylindric Li-ion batteries for validation.

Recently, Ostanek et al. [20,21], as well as Parhizi et al. [22], reused a combination of Hatchard's [17], Kim's [18], and Coman's [19] models to accelerate and improve the numerical solution procedure to give better consideration to the stiff nature of those reaction equations. Further, they extend the model by involving battery vent gas generation and venting.

Also, Sorensen et al. [23], García et al. [10], and Sun et al. [24] successfully modeled the TR-based Arrhenius reaction rate. Instead of modeling the SEI, cathode, anode, and electrolyte, they take advantage of splitting TR into multiple stages, similar to Ostanek et al. [5], and assigning one reaction rate per stage.

Each of the publications named above employs an Arrhenius-type reaction rate, which is typically described as follows:

$$\dot{R}_{i,j}(t) = A_{i,j} \cdot \exp\left(-\frac{E_{a,j}}{R_u T_{Cell,i}}\right) \cdot Y_{i,j} \tag{5}$$

where the index i refers to the finite volume (FV) inside the discretized battery cell active material, as shown in Figure 2, where j is the index of the reactant or stage, A_j is the pre-exponential factor of the reaction, R_u is the universal gas constant, $E_{a,j}$ is the activation energy, and Y_j gives the concentration of the reactant in the battery cell's active material.

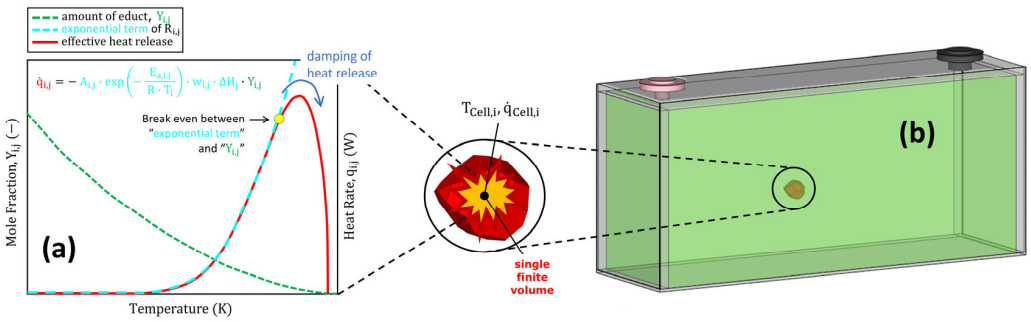

Figure 2. (**a**) Schematic of the exothermic thermal runaway heat release rate, $\dot{q}_{Cell,i}$, as a function of local active material temperature, $T_{Cell,i}$, and (**b**) schematic finite volume (FV) discretization of the battery cell active material used in this study (illustrated for a prismatic battery cell).

The consumption of the reactant is as follows:

$$\frac{\partial Y_{i,j}}{\partial t} = -\dot{R}_{i,j} \tag{6}$$

The heat source resulting from each reaction is as follows:

$$\dot{q}_{i,j}(t) = w_j \cdot \Delta H_j \cdot \dot{R}_{i,j} \tag{7}$$

where w_j is the specific mass of reactants and ΔH_j is the specific enthalpy of the reaction.

Eventually, the heat released due to thermal runaway per finite volume, i, inside the discretized battery cell active material, as shown in Figure 2, totals to the following:

$$\dot{q}_{Cell,i}(t) = \sum_{j=0}^{M} \dot{q}_{i,j}(t) \tag{8}$$

where M is the total number of reactions considered.

A_j, $E_{a,j}$, and ΔH_j for each of the reactions could be determined via accelerating rate calorimeter (ARC) and differential scanning calorimeter (DSC) experiments, as presented by MacNeil [25], Peng [26], and Abada [27] for LCO, NMC, and LFP cathodes. The materials like the cathode, anode, and electrolyte needed for such an analysis could be extracted via a teardown from the device under test (DUT).

The advantage of the model presented in Equations (5)–(8) compared to the Gaussian TR model of Section 2.1 is that the competition of the increasing battery cell temperature (exponential term) and the consumption of each reactant, $Y_{i,j}$, inside each FV, i, of the battery cell active material is accounted for, as shown in Figure 2. While TR progresses, the battery cell temperature, $T_{cell,i}$, increases due to the exothermal heat from each reaction, $\dot{q}_{i,j}$. Due to the increasing battery cell temperature, the exponential term of the reaction rate is further amplified, which in turn amplifies the consumption of the reactant. At a certain level of reactants consumed, the damping nature of $Y_{i,j}$ in Equation (5) dominates over the exponential term, which causes the heat release to drop with increasing battery cell temperature.

2.2.1. One-Step Reaction Rate TR Models

Instead of considering each exothermic reaction for cathode, anode, SEI, electrolyte, and ISC, MacNeil et al. [25] offer a lumped one-step model based on a reaction rate approach as follows:

$$\dot{q}_{Cell,i}(t) = A \cdot \alpha \cdot (1-\alpha) \cdot (-\ln(1-\alpha)) \cdot \exp\left(-\frac{E_a}{R_u T_{Cell,i}}\right) \tag{9}$$

Alternatively, Kim et al. [28] adopt the negative solvent reaction equation of Hatchard et al. [17] and use it as a lumped one-step formulation as follows:

$$\dot{q}_{Cell,i}(t) = A \cdot \alpha \cdot (1-\alpha) \cdot \exp\left(-\frac{E_a}{R_u T_{Cell,i}}\right) \cdot \exp(-B\alpha) \tag{10}$$

The latter is used successfully to predict battery TR and venting.

2.2.2. Current One-Step Reaction Rate TR Model

From the current research activities, a new form for a one-step reaction rate TR model is proposed, hereafter named "Reaction rate model". The model presented here combines the reaction rate model in Section 2.2 with the staging of the TR process as proposed by Citarella et al. [4], as shown in Section 2.1. Thus, the current TR model is written as follows:

$$\dot{R}_{stage,i}(t) = A_{stage} \cdot \exp\left(-\frac{E_{a,stage}}{R_u T_{Cell,i}}\right) \cdot Y_i \tag{11}$$

with

$$\dot{q}_{i,stage}(t) = \Delta H_{stage} \cdot \dot{R}_{stage,i}(t) \tag{12}$$

Note the consideration of Y_i in Equation (11), which accounts for the consumption of the reactant during TR, as discussed in Section 2.2. For Equation (11), $Y_i(t = 0) = 1$, which reduces to zero when the TR reaction ends. The consumption of the reactant, Y_i, is modeled according to Equation (6).

Parameters like the pre-exponential factor, A_{stage}, and the activation energy, $E_{a,stage}$, refer to the cell active material, which is treated in this article as a lumped mass. Here, no differentiation between cathode, anode, SEI, or electrolyte is applied.

The model is finally built by superposing each model stage, as shown in Figure 1, under consideration of Equations (11) and (12) as follows:

$$\dot{q}_{Cell,i}(t) = \begin{cases} \dot{q}_{i,stage\ 2} \text{ if } [T_{onset,1} < T_{Cell,i}(t) < T_{onset,2}] \\ \min\left[\dot{q}_{i,stage\ 3a}, \dot{q}_{i,stage\ 3b}\right] \text{ if } [T_{Cell,i}(t) > T_{onset,2}] \end{cases} \tag{13}$$

The stage 2 model describes the same physical phenomena as the first part of the Gaussian model in Section 2.1.

The stage 3a model describes the very initial onset of the exothermal reaction of the cathode materials with the electrolyte and the heat due to ISC. Stage 3a models the initial period of the second part of the Gaussian model discussed in Section 2.1.

The stage 3b model continues stage 3a. Figure 1 identifies a limitation of the exothermal heat release during the ARC test for the current DUT. This finding is confirmed by other published data, like Golubkov et al. [14] and [7], for 18650 Li-ion battery cells with LCO, NMC, LFP, and NCA cathodes. Also, García et al.'s [10] data for 18650 and 21700 battery cells with NCA and NMC cathodes confirms this finding. The damping of the TR heat release, which is visible in Figure 1 for cell temperatures > 500 °C, is inherently modeled via the consumption of the reactant.

The major advantage of Equation (13) is that the TR mechanism of stages 2, 3a, and 3b is uncoupled from one another. This allows us to identify the reaction parameters individually per stage. Discontinuities, as indicated in Figure 1b, could be explicitly allowed, which enhances the correlation of test data and the TR model parameter dramatically.

The most convenient way to transfer Equation (13) into a commercial solver is tabled data. In the present 3D CFD analysis, Equation (13) is evaluated via a global formula in AVL FIRE™ M 2021.2, as shown in Section 1. The model is plotted along with test data in Figure 1a.

2.2.3. Generalization Across Cell Chemistries

Golubkov et al. [7] observed stage-wise trends for cylindric 18650 cells with LCO, NCA, and LFP cathodes, similar to those captured in this study for the battery skin temperatures and temperature rate profiles, as shown in Figure 1. This reported data supports the assumption that the proposed multi-stage reaction rate model may also be transferable to these cathode chemistries and is not unique to the NMC721 studied here.

2.3. Identification of Reaction Parameters

To identify the stages of thermal runaway and their parameterization for the reaction rate model in Equation (13), initially, the measured cell skin temperatures must be transferred to temperature rates via central differencing as follows:

$$\left.\frac{dTT_{TC,max}}{dt}\right|_n = \frac{T_{TC,max}^{n+1} - T_{TC,max}^{n-1}}{t^{n+1} - t^{n-1}} \tag{14}$$

where n indexes the discrete test time samples. $T_{TC,max}$ is evaluated from the monitored cell skin temperatures as follows:

$$T_{TC,max} = \text{top8}(T_{TC,1}, \ldots, T_{TC,16}) \tag{15}$$

During the ARC experiment, temperature is sampled at 1 kHz. To suppress noise in the measured data, a trailing moving average filter is applied to the temperature rate signal evaluated by Equation (14). Stage onsets are detected when the windowed rate first exceeds the prescribed thresholds ε as follows:

$$n_{onset} = \min\left\{ n > k : \frac{1}{k}\sum_{j=0}^{k-1} \left.\frac{dT_{TC,max}}{dt}\right|_{n-j} \geq \varepsilon \right\} \tag{16}$$

The corresponding onset temperatures are identified as follows:

$$T_{onset} = T_{TC,max}(n_{onset}) \tag{17}$$

The inputs for ε and k and the results for T_{onset} are summarized in Table 1. The reaction rate parameters A_{stage} and $E_{a,stage}$ in Equation (11) are estimated from ARC test data via linear regression as follows:

$$\ln\left(\frac{dT_{TC,max}}{dt}\right) \approx -\frac{E_{a,stage}}{R_u}\cdot\frac{1}{T_{TC,max}} + \ln\left(\Delta T \cdot A_{stage}\right) = -\frac{\text{slope}}{T_{TC,max}} + b \tag{18}$$

Table 1. Summary of the reaction rate parameters A, E_a, and ΔH identified from the ARC results of the NMC721 pouch cell (Figure 1). These parameters enter the reaction rate TR model via Equations (11) and (12), and they are valid for SoC = 100% and SoH = 100%.

Stage	ε	k	T_{onset}	ΔT	Slope	b	A	E_a	ΔH	R^2	RMSE	σ
	[K/s]	[–]	[°C]	[K]	[K^2/s]	[K/s]	[1/s]	[J/mol]	[J/m^3]	[–]	[–]	[–]
2	0.033	100	146	50	$-1.418 \cdot 10^4$	29.27	$1.027 \cdot 10^{11}$	$1.179 \cdot 10^5$	$1.575 \cdot 10^8$	0.35	1.00	1.00
3a	0.15	100	196	120	$-5.756 \cdot 10^3$	15.37	$3.950 \cdot 10^4$	$4.786 \cdot 10^4$	$3.780 \cdot 10^8$	0.77	0.40	0.40
3b	245	20	315	511	0	5.63	$5.479 \cdot 10^{-1}$	0	$1.610 \cdot 10^9$	−4.17	2.50	1.10

Equation (18) is successfully applied by Shelkea et al. [29] for a 21700 battery cell, Sorensen et al. [23] for 18650 pouch battery cells, and by García et al. [10] for 18,650 and 21,700 battery cells with NCA and NMC cathode chemistries at different SoCs and states of health (SoHs). Equation (18) assumes that the battery cell energy balance can be approximated by a quasi-adiabatic condition during TR. Thus, the exponential increase in the battery cell temperature is assumed to be far greater than the heat dissipation.

Equation (18) allows us to determine $E_{a,stage}$ from its slope as follows:

$$E_{a,stage} = -\text{slope}\cdot R_u \tag{19}$$

and A_{stage} from its intercept, b, as follows:

$$A_{stage} = \frac{\exp(b)}{\Delta T} \tag{20}$$

The enthalpy of the reaction, ΔH_{stage}, needed for Equation (12) is evaluated as follows:

$$\Delta H_{stage} = \frac{c_p \cdot m \cdot \Delta T}{Vol_{Cell}} \tag{21}$$

where c_p is the specific heat capacity of the battery cell active material, m is the mass of the battery cell, and ΔT is the temperature difference per TR stage estimated as follows:

$$\Delta T = T_{onset,stage\ m} - T_{onset,stage\ m-1} \tag{22}$$

Here, m indices the thermal runaway stage, e.g., 2, 3a, or 3b. The final model parameters employed for Equation (13) are documented in Table 1 and Figure 1. As these parameters are determined from the skin temperatures of the DUT recorded during the ARC test (see Section 2.3), it must be acknowledged that they are bound to the test conditions, battery cell chemistry, battery cell SoC (here 100%), and SoH (here 100%), which limits the model's predictive capability to prior parameter identification from experimental data.

2.3.1. Expected Impact of SoH and SoC on the Reaction Parameters

Across multiple chemistries (NMC, NCA, LFP, LCO, and LMO) and cell formats (prismatic, pouch, cylindric), Han et al. [9], Garcia et al. [10], Willstrand et al. [11], Essl et al. [12], Bugryniec et al. [13], Golubkov et al. [14], and Pfrang et al. [2] found a consistent trend of reduced T_{onset}, increased T_{max}, and increased temperature rates (dT/dt) with increasing SoC. Willstrand et al. [11] quantified T_{onset} to decrease by ~18 °C per 25% SoC increase. Garcia et al. [10] associate this trend with faster early exothermic reactions due to increased lithium at the anode. According to Golubkov et al. [14], this trend is found to be drastically enhanced under overcharge; LFP cells are found to exhibit a similar but less pronounced effect on SoC. Essl et al. [12] and Bugryniec et al. [13] identified battery cells (LFP, NMC, and LMO chemistries) that did not enter thermal runaway for SOC $\leq$ 30%.

Regarding state of health, Han et al. [9] show that cycling-aged prismatic LCO cells (≈90% SOH) trigger thermal runaway earlier in time than fresh cells at the same SOC, linking this to SEI instability and structural degradation of the electrodes. They also report that aging reduces peak dT/dt at 100% SOC (less active material → milder exotherm), whereas at 50% and 0% SOC, aged modules exhibit higher peak dT/dt, plausibly due to unstable SEI, structural changes at the negative electrode, which causes heat accumulation that delays but then intensifies the reaction heat release. García et al. [10] highlight stronger dispersion towards lower onset temperatures and reduced exothermic heat release with ageing for cylindric 18650 and 21700 NCA and NMC cells, which they correlate with capacity fading from SEI growth.

Consistent with the observed SoC and SoH trends, a reduction in the exothermic temperature rate, dT/dt, as shown in Equation (18), implies a smaller intercept b, i.e., a smaller A_{stage} according to Equation (20), provided the slope remains approximately constant. Likewise, an increase in the onset temperature, T_{onset}, with decreasing SoC or increasing SoH, implies a smaller A_{stage} under the same assumption. In case the slope of the temperature rate, dT/dt, would flatten, Equation (19) implies a decrease in $E_{a,stage}$.

To recalibrate the reaction rate model in Equation (13) for the DUT for states other than 100% SoC and 100% SoH, ARC data must be acquired at the SoC and SoH of interest, and the procedure in Equation (14) to (22) must be repeated. If ARC testing is limited, available

data may be adjusted for T_{onset} following the approach of Willstrand et al. [11]. A rigorous evaluation of such surrogate adjustments is beyond the scope of this work and remains future research.

2.3.2. Expected Impact of the Cell Format on the Reaction Parameters

As the ARC test data is sampled on the skin of the NMC721 pouch battery cell, the result of Equations (19) and (20) must be considered as an initial guess due to the aluminum-laminated pouch between the thermocouples and the active material, which acts as a thermal resistance. Subsequently, A_{stage} and $E_{a,stage}$ must be refined using a 3D CFD CHT simulation (see Section 4.2). As the aluminum-laminated pouch typically spans 100–200 µm in thickness for automotive pouch battery cells, its thermal resistance can be considered very small for the DUT studied here. In fact, almost no calibration of the parameters given in Table 1 and Figure 1 was needed in this study. Comparing prismatic hard case battery cells versus the pouch, both batteries have the same nominal capacity of 60 Ah, NMC622 cathodes, SoH = 100%, SoC = 100%, and a graphite anode, but different electrolyte mixtures. Essl et al. [15] identify ≈ 5–7% lower T_{max} and T_{onset} for the hard case cell compared to the pouch cell. This finding implies that reaction rate parameters require calibration for setups where thermal resistance exists between the thermocouple and the battery's active material rather than being inferred directly from skin temperature measurements.

2.4. Estimation of Battery Thermal Energy

The thermal energy released, Q_{Cell}, inside of a battery cell during TR is defined as follows:

$$Q_{Cell} = \sum_{t=0}^{t_{END}} \sum_{i=0}^{N} \dot{q}_{Cell,i}(t) \cdot Vol_i \cdot \Delta t \tag{23}$$

where N is the total number of FV inside the discretized battery cell active material. Q_{Cell} must be assumed to depend on the battery cell chemistry, the cell's electric capacity, C, its state of charge, SoC, and the battery cell voltage, U. According to Hoelle [30], the total amount of thermal energy stored in a battery cell is as follows:

$$Q_{total} = Q_{Cell} + Q_{Vent} + Q_{Particle} \tag{24}$$

with a regression for Q_{tot} identified as follows:

$$Q_{tot} \approx C \cdot 19.45 \frac{kJ}{Ah} = E_{Cell} \cdot 1.29 \; \forall \; 8 \text{ Ah} < C < 145 \text{ Ah} \tag{25}$$

where $E_{Cell} = C \cdot U \cdot 3600$. The scattering of single test results compared to Equation (25) is found by Hoelle [30] to vary between $E_{Cell} \cdot 1.2 < Q_{tot} < E_{Cell} \cdot 1.72$. For Q_{Cell}, a similar regression is presented by Hoelle [30] as follows:

$$Q_{Cell} \approx C \cdot 10.76 \frac{kJ}{Ah} = E_{Cell} \cdot 0.71 \; \forall \; 8 \text{ Ah} < C < 145 \text{ Ah} \tag{26}$$

The scattering of single test results compared to Equation (26) is found by Hoelle [30] to vary between $E_{Cell} \cdot 0.5 < Q_{tot} < E_{Cell} \cdot 1.1$. Considering the mass ejected from the battery cell during TR, meaning particulate matter and vent gas, Hoelle [30] finds the following:

$$Q_{Cell} \approx C \cdot 19 \frac{kJ}{Ah} \cdot \frac{m_{Cell,after}}{m_{Cell,before}} \tag{27}$$

Hoelle [30] derived these findings from testing 50 prismatic battery cells triggered via nail penetration in an inert environment, with cell capacities varying from 8 and 145 Ah and having NMC and NCA cathode materials.

By summarizing Equations (25)–(27) for the DUT used in this analysis, as shown in Section 3, the above calculus gives the following:

$$1.20\ \text{MJ} < Q_{tot} < 1.72\ \text{MJ} \tag{28}$$

and

$$0.50\ \text{MJ} < Q_{Cell} < 1.10\ \text{MJ} \tag{29}$$

The total energy, Q_{Cell}, released inside the DUT in the 3D CFD simulation, is affected by the quality of the TR model parametrization. For well-posed TR model parameters, Q_{Cell} predicted by the 3D CFD simulation is expected to satisfy Equation (29). From the 3D CFD simulation results, a regression for Q_{Cell} versus battery cell capacity is derived, which is plotted in Figure 3b. The regression is identified as follows:

$$Q_{Cell} \approx 0.82 \cdot E_{Cell} = 0.82 \cdot C \cdot U \cdot 3600 \tag{30}$$

Equation (30) is developed from available 3D CFD simulation results of the DUT analyzed in the context of this article (see Section 3), a 5 Ah 21700 cylindric cell (m = 62 g), a 151 Ah (m = 1.78 kg), and a 246 Ah prismatic battery cell (m = 3.5 kg). Each of these battery cells uses NMC as the cathode material. The 3D CFD CHT simulation models for each of these battery cells are built similarly to the ARC test model, as described in Section 4.2. In these simulations, the TR models in Sections 2.1, Polygon Resampling, and 2.2.2 are used.

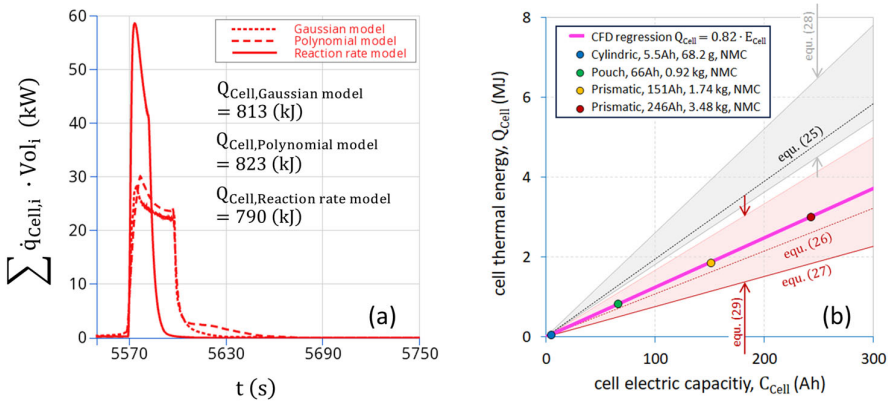

Figure 3. (**a**) Comparison of the exothermic heat release rate, $\dot{q}_{Cell,i}$, and accumulated thermal energy, Q_{cell}, during thermal runaway for each TR model, (**b**) summary of Q_{cell} versus battery cell electrical capacity across various battery cell formats and sizes.

Following Hoelle [31], mass loss during TR could significantly affect the simulation results, and thus also Q_{Cell}. Figure 3a summarizes the total heat release predicted by the 3D CFD model used in this study (see Section 4), which neglects mass loss of the DUT (see Section 3) due to vented gas and ejected particles. Thus, the CFD model also neglects the enthalpy removal associated with mass loss (see Equation (24)). In contrast to Figure 3a, Equation (27), which accounts for ejected battery material, yields $Q_{Cell} \approx 502$ kJ for the DUT (here $m_{Cell,after} = 0.29$ kg). Hence, the simulation overestimates Q_{Cell} by ≈ 288 kJ.

To check the order of magnitude implied by Equation (27), the difference in sensible energy required to heat the fresh DUT versus the abused (lighter) DUT is estimated as follows:

$$\Delta Q_{Cell} \approx c_p \cdot (m_{Cell,before} - m_{Cell,after}) \cdot (T_{max} - T_{onset,2}) = 393\ \text{kJ} \tag{31}$$

with c_p according to Table 2, $T_{onset,2} = 146$ °C according to Table 1, and $m_{Cell,before} = 0.92$ kg and $T_{max} = 826$ °C (both given in Section 3).

Table 2. Thermophysical properties at 20 °C for components in the 3D CFD ARC test model, the 3D CFD 4S4P battery module model, respectively.

Part	Base Material	Thermal Conductivity (λ)	Heat Capacity (c_p)	Density (ρ)
		[W/mK]	[J/kgK]	[kg/m^3]
Jig, Module Case, Cold Plate	Stainless steel	21	430	7770
Copper Plate	Copper	400	384	8960
Mica Sheet	Mica	0.15	866	2150
DUT	NMC721	x = 24 y = 24 z = 1	1050	3200
Wool	Ceramic fiber	0.2	1030	96
Thermal Paste	Silicone	2	770	2550
Thermal Pad	Aerogel	0.1	1100	160

Thus, the present 3D CFD model overestimates the energy released per battery cell during thermal runaway by ≈288–393 kJ, as the full active inventory remains available for exothermic reaction.

3. Battery Overheat Test

The thermal runaway behavior of the battery is evaluated using an accelerating rate calorimetry (ARC) test. This test is conducted within a sealed stainless-steel reactor with a capacity of 120 L. The ARC test is performed twice: once with the reactor pre-filled with nitrogen (N2) to inhibit combustion of the battery vent gases and second with the reactor filled with ambient air.

The battery cell skin temperature is tracked at 16 positions on the pouch foil. The vent gas temperature is measured at 10 locations inside the reactor. Voltage and charge current are also measured during the test.

The battery cell skin and vent gas temperatures are recorded using Type K (Class 2) glass fiber insulated flat pair thermocouples (IEC 60584-3:2021. *Thermocouples—Part 3: Extension and compensating cables—Tolerances and identification system*. International Electrotechnical Commission), having a tolerance of ±2.5 °C in the range of −40 °C to 1200 °C. Temperature sensing is created by wire twisting.

The cell is inserted into a sample holder, as shown for the 3D CFD model setup in Figure 4. To imitate the installation in a stack or a module, the device under test (DUT) is supplied with an initial compression force.

The DUT is an NMC721 pouch cell with 66 Ah nominal capacity and 4.2 V maximum open circuit voltage. Its dimensions are 318 × 92 × 10 mm, and its weight before the test is 0.92 kg. The battery cell state of charge (SoC) before the test is 100%, which is a thermal worst case; see also Section 2.2.2.

The cell is triggered for thermal runaway via continuous external heating. Therefore, 2 × 500 W heaters are applied at each jig, top, and bottom (see also Figure 4). The external heating is adjusted to target a battery cell skin heating rate of ~1.5 °C/min.

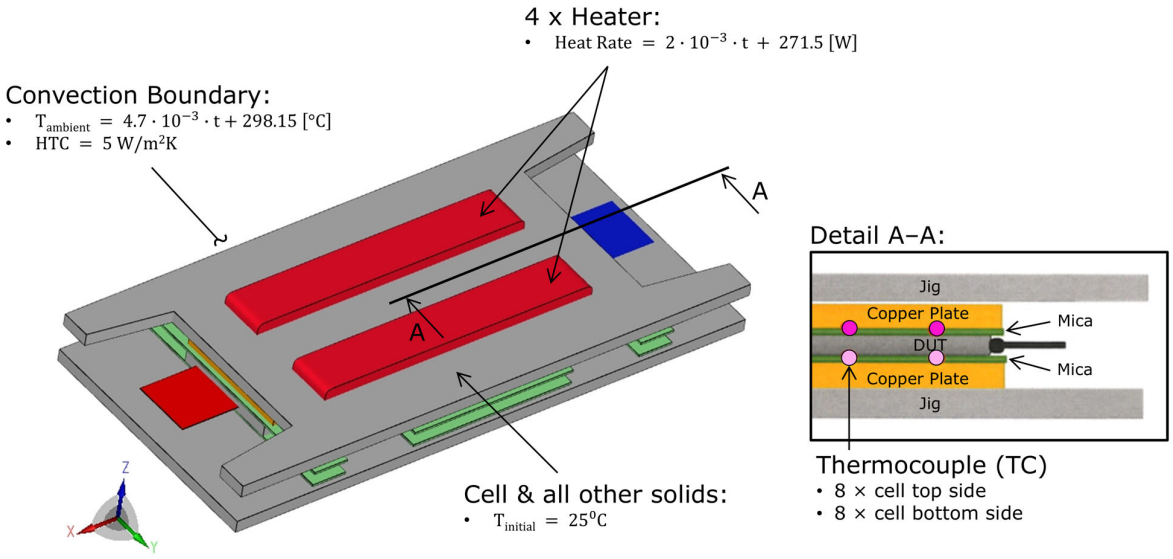

Figure 4. Schematic of the accelerating rate calorimetry (ARC) test setup and the corresponding 3D CFD model for the NMC721 pouch battery cell. The 3D CFD model resolves only the cell assembly shown above; all modeled components are treated as solids. The ARC reactor gas is replaced by a convective boundary condition (prescribed ambient temperature and heat transfer coefficient).

Test Results

At the start of the test, the reactor and the battery cell are homogenously conditioned at 28 °C. At ~3100 s, first venting occurs. At ~5567 s, the cell voltage drops below 50% of its nominal level. At the same time, the gas temperature becomes >200 °C and the gas pressure starts to increase rapidly. At ~5570 s, the battery skin temperature turns > 200 °C. Rapid thermal runaway occurs. At ~5575 s, the last cell skin thermocouple signal turns > 200 °C. At ~5590 s, the maximum local cell skin temperature of ≈826 °C (for N2 atmosphere) and ≈839 °C (for air) occurs.

4. CFD Results and Discussion

4.1. Solver and CFD Model

The solver of choice is the commercial software AVL FIRE™ M 2021.2. The solver uses a finite volume (FV) approach to discretize the conservation equations for a continuum like gas, liquid, or solid.

The CFD models analyzed in this study are three-dimensional (3D) conjugate heat transfer (CHT) replicates of a battery ARC test, as shown in Figure 4, and a fictitious 4S4P battery module, as discussed in Section 4.3. The conservation of thermal energy inside the solid materials is solved in the temperature formulation of the energy equation as follows:

$$\rho \cdot c_p \cdot \frac{\partial T}{\partial t} = \nabla \cdot \lambda \nabla T + \dot{q}_{Cell} \quad (32)$$

where ρ, c_p, and λ are the density, specific heat capacity, and thermal conductivity of the solid materials. T is the temperature of the solid material and $\dot{q}_{Cell}$ is the scalar heat source from TR and heat diffusion, which is modeled according to Fourier's law of conduction.

The reactant, Y, feeding the thermal runaway reaction, is implemented in the AVL FIRE™ M solver using a passive scalar transport equation. The consumption of Y is modeled according to Equations (3) and (6).

The heat release from TR is evaluated via a global formula, which is evaluated before the start of the iteration for each time step using the results available from the previous time step as input data. The latter linearizes the coupling of the bat-

tery cell active material temperature, $T_{Cell,i}(t)$, and the reaction rate of the model as given in Equations (1), (2), (4), and (13), which gives a positive effect on the stability of the simulation.

The models analyzed in the context of this paper show moderate to non-stiff behavior. Thus, no special numerical treatment for the stiff reaction rate differential equations, as discussed by Ostanek et al. [20] and Parhizi et al. [22], is needed. The step size for time marching is estimated from linear stability analysis as follows:

$$\Delta t = \min\left(\frac{\rho_i \cdot c_{p,i} \cdot vol_i^{2/3}}{\lambda_i}, \frac{\rho_i \cdot c_{p,i} \cdot T_i}{\dot{q}_{Cell,i}}\right) \quad (33)$$

and is limited to 0.005 s < Δt < 10 s. The first term of Equation (33) gives the contribution from the diffusive heat transport inside the solid materials, and the second term gives the limitation coming from the local magnitude of the heat rate introduced in the CFD domain. The index i refers to each finite volume (FV) in the CFD mesh.

Limitations of the CFD Model

In each CFD model analyzed in this study, all materials are treated as solid components having literature-based material properties, as shown in Table 2. As a result, potential temperature-dependent variations of the material properties are not explicitly accounted for.

Steel and copper properties are adopted from the VDI-Wärmeatlas [32], and supplier-specific material properties are used for ceramic fiber (Refractory Ceramic Fiber), mica (Insulectric), and aerogel (Aspen Aerogel). Also, the battery cell is modeled as a solid material, which agrees with the modeling reported by Citarella et al. [4], Ostanek [5], and Hoelle et al. [31]. The battery's material properties are adopted from supplier information (LG), and its density is derived from the analysis of the fresh battery volume and weight, as shown in Section 3. The magnitude of battery properties used in this study compares well with data reported by Ostanek [5] (cp = 950 J/kgK) and Koller et al. [33] ($\lambda_x = \lambda_y = 1.78 - 32$, $\lambda_z = 0.15 - 2.59$ W/mK and cp = 970–1020 J/kgK).

Consequently, phase change and gas propagation inside the battery active material are currently not modeled. Vent gas generation, its ejection, the release of particulate matter, and the resulting loss of cell mass during thermal runaway are not modeled in this study. In principle, these phenomena could be represented by volumetric source terms within the active material domain, but this is beyond the scope of the present work. The implications of this simplification are discussed in detail at the end of Section 2.4.

4.2. Single-Cell Thermal Runaway

To test the thermal runaway (TR) models introduced in Sections 2.1, Polygon Resampling, and 2.2.2, the ARC test in Section 3 is replicated in AVL FIRE™ M as a 3D CFD CHT model, as shown in Figure 4. The solid parts of the ARC test assembly, like the copper plates, mica sheets, steel jigs, and the battery cell and its tabs, build the 3D CFD model. The reactor structure and the gas atmosphere inside the reactor are not modeled.

The heat transfer from the battery cell to the reactor gas is modeled via a convection boundary condition (BC). The reactor gas reference temperature for convection is chosen to be the recorded gas temperature from the test. The convective heat transfer coefficient is defined as 5 W/m^{2}K (free convection). All material properties used in the CFD model are given in Table 2. Due to the lack of temperature-dependent data, the material properties refer to 20 °C.

To correlate the 3D CFD temperature predictions to the ARC test, monitoring points are positioned in the 3D CFD model at the same positions as the thermocouples (TCs), which record the cell skin temperatures in the ARC test. To evaluate the quality of the 3D

CFD predictions, the cell skin temperatures from the test and the CFD simulation must at least match T_{max}, $T_{onset,1}$, and $T_{onset,2}$, the times when $T_{onset,1}$ and $T_{onset,2}$ occur, and the temperature rates evaluated from the cell skin temperature.

In Figure 5a–c, the monitored cell skin temperatures predicted by the Gaussian (Section 2.1), the polynomial (Section Polygon Resampling), and the reaction rate model (Section 2.2.2) are plotted with the data from the ARC test. The CFD data is plotted in magenta, and the test data are in gray. Each model adequately predicts the onset of TR. Also, the predicted maximum cell skin temperature of 826 °C agrees well with the test. One feature of the Gaussian and the polynomial model, which separates them from the reaction rate model, is that the monitored cell skin temperature is pointed towards its maximum. The reaction rate model predicts a smoother transition near the maximum cell skin temperature, which compares better to the test.

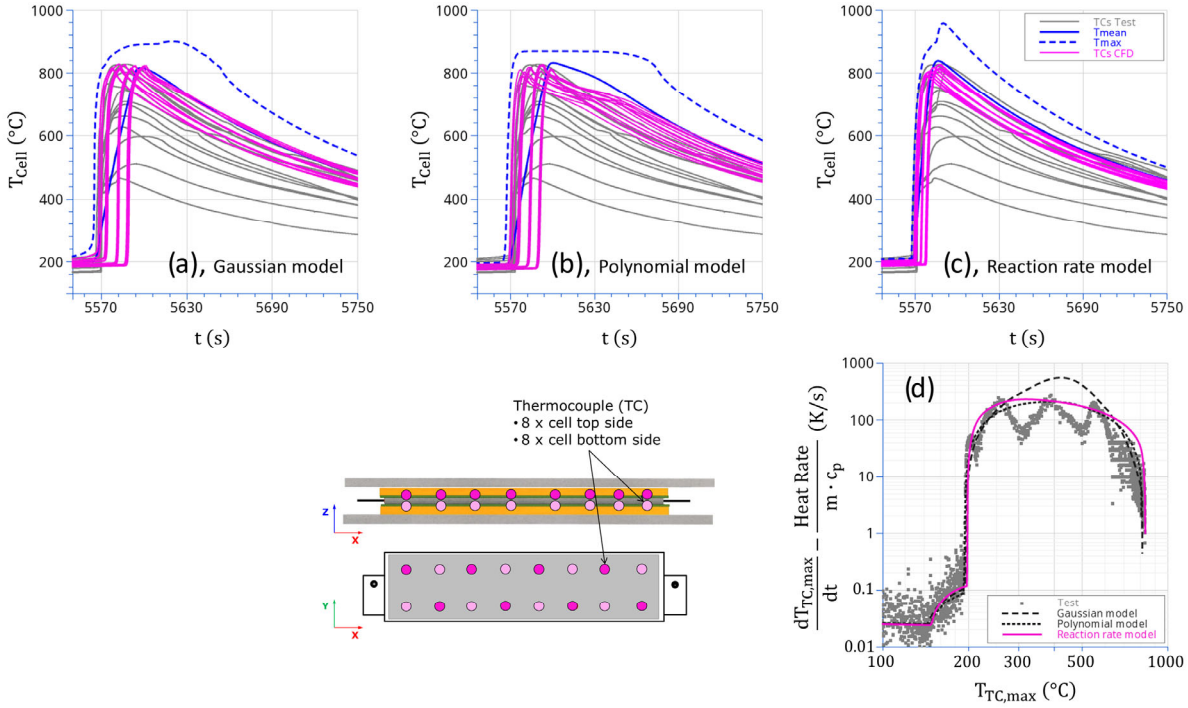

Figure 5. Predicted battery cell temperatures for (**a**) the Gaussian TR model, (**b**) the polynomial TR model, (**c**) the reaction rate TR model, (**d**) and the comparison of temperature rates, dT/dt, for the ARC test and all three TR models evaluated by Equations (15) and (16).

Figure 5d shows the temperature rate calculated from the monitored cell skin temperatures for the Gaussian, the polynomial, and the reaction rate model according to Equations (14) and (15). The magenta line gives the temperature rate of the reaction rate model, which is also discussed in Figure 5c.

In Figure 3a, the total heat release inside the battery active material is plotted. Remarkably, the polynomial model exhibits a plateau-like state from t = 5591 to 5607 s. In Figure 6, it is identified that the heat release predicted by the polynomial model locally drops to zero once the local cell temperature reaches 850 °C, even though not all reactants, Y, are yet consumed. This is because the polynomial model drops to zero at T_{max} = 850 °C, as shown in Figure 1. The heat release locally increases again as soon as the local cell temperature drops below 850 °C. This process repeats until all available reactants, Y, are consumed. This model feature causes an unplausible gradient of the predicted cell skin temperatures during the cooling period (stage 4), as shown in Figure 5b, at 5620–5650 s. For the reaction rate model this effect is not present at all as shown in Figure 7.

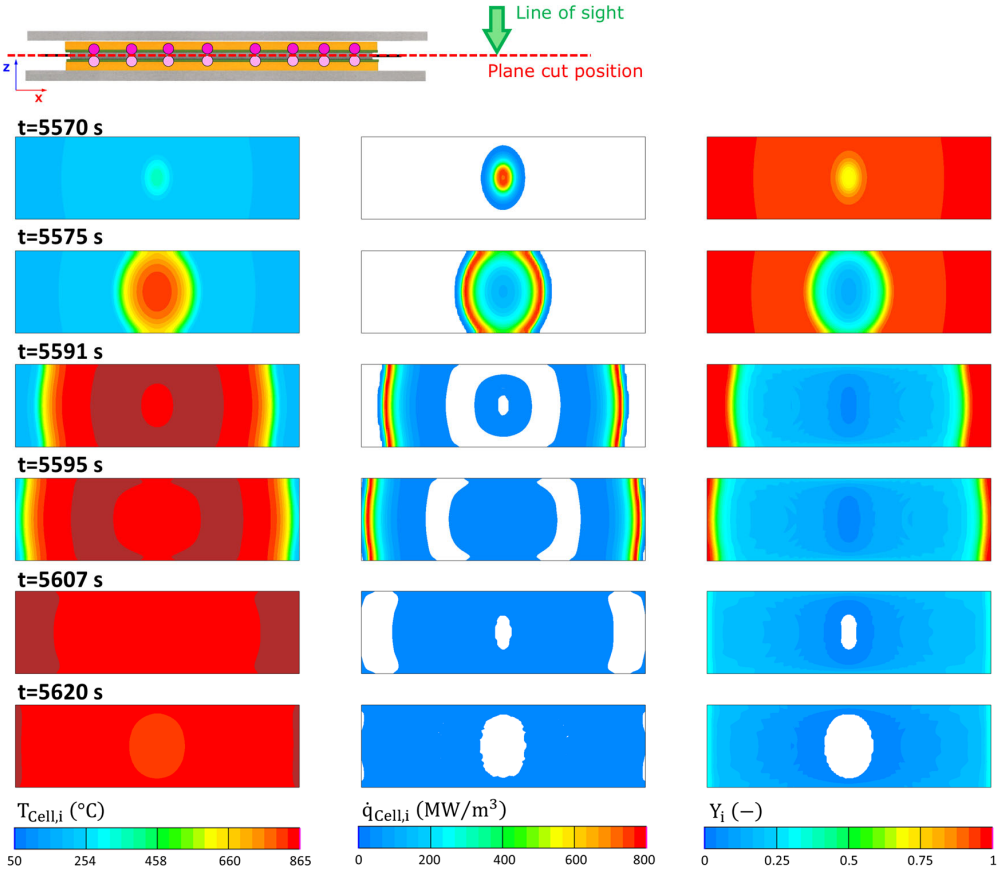

Figure 6. Three-dimensional CFD predictions for the ARC test using the polynomial TR model (Section Polygon Resampling), (**left**) the battery cell temperature, (**middle**) the thermal runaway heat release rate, (**right**) and the remaining mass fraction of reactant inside the battery cell.

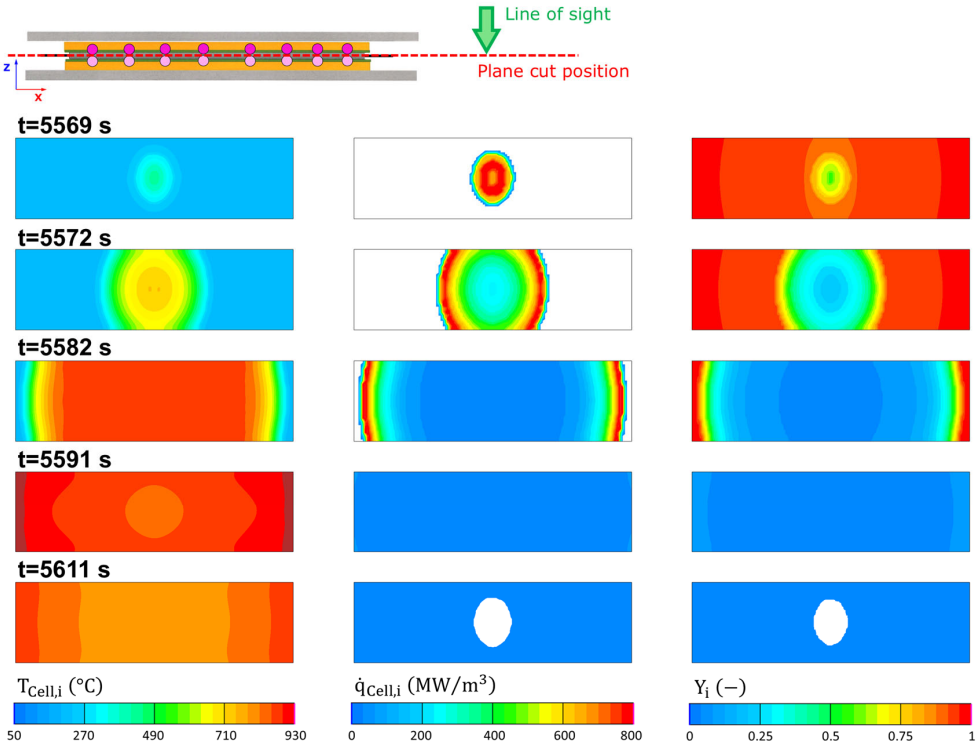

Figure 7. Three-dimensional CFD predictions for the ARC test using the polynomial TR model (Section 2.2.2), (**left**) the battery cell temperature, (**middle**) the thermal runaway heat release rate, (**right**) and the remaining mass fraction of reactant inside the battery cell.

4.3. Module Thermal Propagation

To put the Gaussian (Section 2.1), the polynomial (Section Polygon Resampling), and the ration rate TR model (Section 2.2.2) in the context of thermal propagation (TP), these models are tested on a 3D CHT CFD model for a 4S4P battery module, as shown in Figure 8. The design of the battery module is fictitious, and it uses the current DUT, as shown in Section 3, as the battery cell. Thus, the TP analysis shown here does not have any test data for reference.

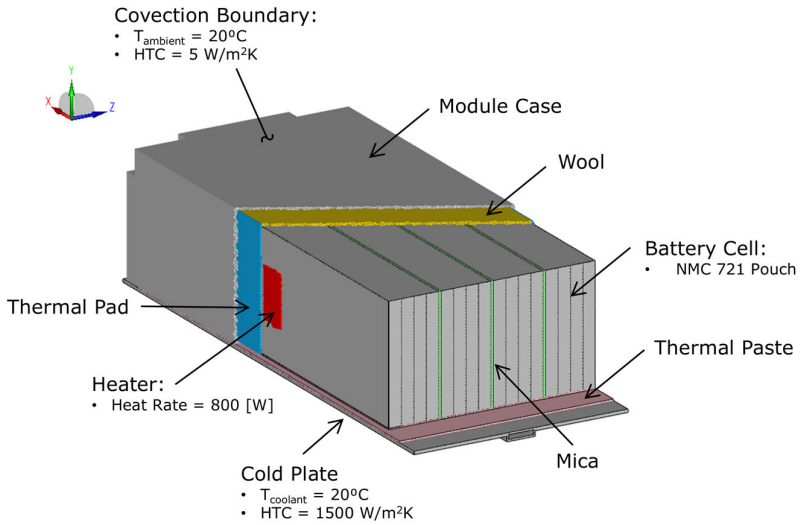

Figure 8. Schematic of the 3D CFD model of the 4S4P pouch cell battery module with a bottom cooling plate and a 25 × 50 mm heater used to initiate thermal runaway. All shown components are modeled as solids; the heat exchange with the surrounding air and the water/glycol 50/50 vol% is prescribed via convective boundary conditions.

TP is simulated under stagnant and active liquid cooling from a bottom cooling plate. For active coolant flow, the cooling heat transfer is replaced by a convective boundary condition, which uses 20 °C as a bulk coolant reference temperature and 1500 W/m^{2}K as a heat transfer coefficient. The choice of the heat transfer coefficient is based on the day-to-day experience of 3D CFD CHT simulations for water/glycol (50%/50% mixture) flow in comparable cold plate geometries.

To enable a controlled comparison of thermal runaway models, the 3D CFD setup excludes battery venting to preserve an orderly, conduction-driven, cell-to-cell propagation pattern. Heat input from vent gas may induce spatially irregular triggers, thereby complicating model comparability. The gas-wetted surfaces of each battery cell (≈3% of the outer battery cell surface in the given 4S4P module design) are assigned a convective boundary condition with an ambient temperature of 20 °C and a heat transfer coefficient of 5 W/m^{2}K, representing free convection.

At the start of the 3D CFD CHT simulation, the whole battery module, including all battery cells, is initialized at 20 °C. To trigger thermal runaway, a heating pad is put between the module case and the first battery cell, as shown in Figure 8. Two different heater sizes are simulated: one heater of the size of the pouch battery cell (318 × 92 mm) and a second heater of 25 × 50 mm. Both are 2.5 mm in thickness, and their heating power is 800 W. The heater is switched off as soon as $T_{Cell1,mean}(t) > T_{onset,2}$, as shown in Equation (35).

The choice for the 318 × 92 mm heater is motivated to provide one scenario where the triggered battery cell is heated across its whole lateral surface to allow homogenous heating of the cell's active material. The heating rate of 800 W is chosen to avoid strong temperature gradients inside the battery cell active material and dominate external cooling. As a result,

under active cooling conditions, the first battery cell is triggered for TR at ≈1000 s after the start of external heating for stagnant coolant at ≈500 s. The 25 × 50 mm heater allows for reducing the energy input to the battery needed to trigger TR. The battery cell experiences strong local heating, which enhances TR triggering. As a result, cell 1 is triggered for TR at ~24 s after the start of heating for both stagnant and active coolant conditions.

In total, four TP scenarios (active and passive coolant, large and small heating) are simulated per TR model (Gaussian, polynomial, and reaction rate model). Figure 9a shows 3D snapshots of the evolution of the battery cell temperatures over time for the reaction rate model. Towards the cold plate, the cell temperature peaks at 760 °C for all TR models. The global maximum battery cell temperature occurs near the top of the module case. By construction, the Gaussian and polynomial models cap the peak at ~850 °C, as their exothermic heat release term vanishes beyond this model-specific cutoff, as shown in Figure 1a. The reaction rate model does not impose such a model-inherent limitation on the local cell temperature. As a result, edge cells show local, transient peak temperatures up to ~50 °C higher than in the single-cell ARC test (see Figure 5c), whereas toward the center (cell 8), peaks are up to ~50 °C lower. These deviations reflect position-dependent thermal coupling rather than a global bias of the reaction rate model. As shown in Figure 8, edge cells (1 and 16) are insulated by compression pads on the side adjacent to the module case and by wool along the top edge; central cells (e.g., cell 8) retain wool insulation only at the top, while both large planar faces exchange heat with adjacent cells.

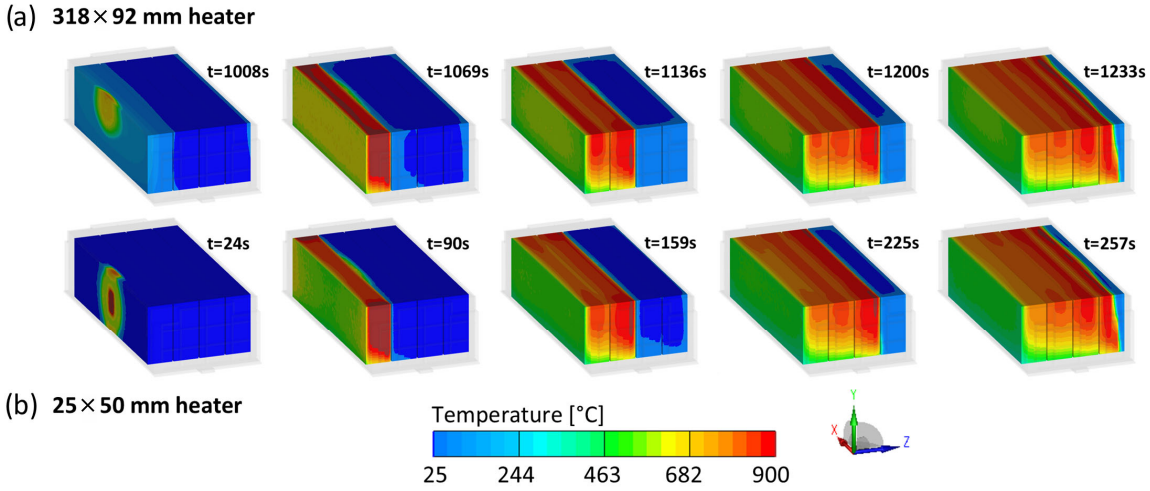

Figure 9. Three-dimensional CFD predictions of the pouch battery cell temperature in the 4S4P module (reaction rate model, active cooling): (**a**) 318 × 92 mm heater, (**b**) 25 × 50 mm heater.

To judge the speed of the heat diffusion from a triggered battery cell into the adjacent module parts and neighboring cells, all cells are evaluated for the time evolution of their local maximum temperature as follows:

$$T_{Cell,max}\left(\vec{x},t\right) = \max(T_{Cell,i}) \tag{34}$$

and for their volumetric mean temperature

$$T_{Cell,mean}(t) = \frac{1}{Vol_{Cell}}\sum_{i=1}^{N} T_{Cell,i}\cdot Vol_i \tag{35}$$

Figure 10a shows $T_{Cell,mean}$ for the reaction rate model for active cooling and the 318 × 92 mm heater used as a trigger. The results for $T_{Cell,max}$ and $T_{Cell,mean}$ of each battery cell are evaluated for $T_{Cell}\left(t_{TR}^{cell}\right) = T_{onset,2}$, where t_{TR}^{cell} is the time when a battery cell

exceeds $T_{onset,2}$; thus, it is triggered for TR. The delta time between two onset events gives the thermal propagation (TP) period, which is evaluated according to Feng [34,35] as follows:

$$TP_{n \to n+1} = t_{TR}^{celln+1} - t_{TR}^{celln} \quad (36)$$

where n is the index of the evaluated cell. The results of Equation (36) are plotted in Figure 10b,c. Active cooling slows down TP at the cell spacer by a maximum of 5 s (cell 12 to 13), and cell-to-cell TP is reduced in the best case by 2–3 s (cell 14, 15, and 16). Further, the reaction rate model is identified to predict about 5–10% faster TP for each scenario simulated on the 4S4P battery module.

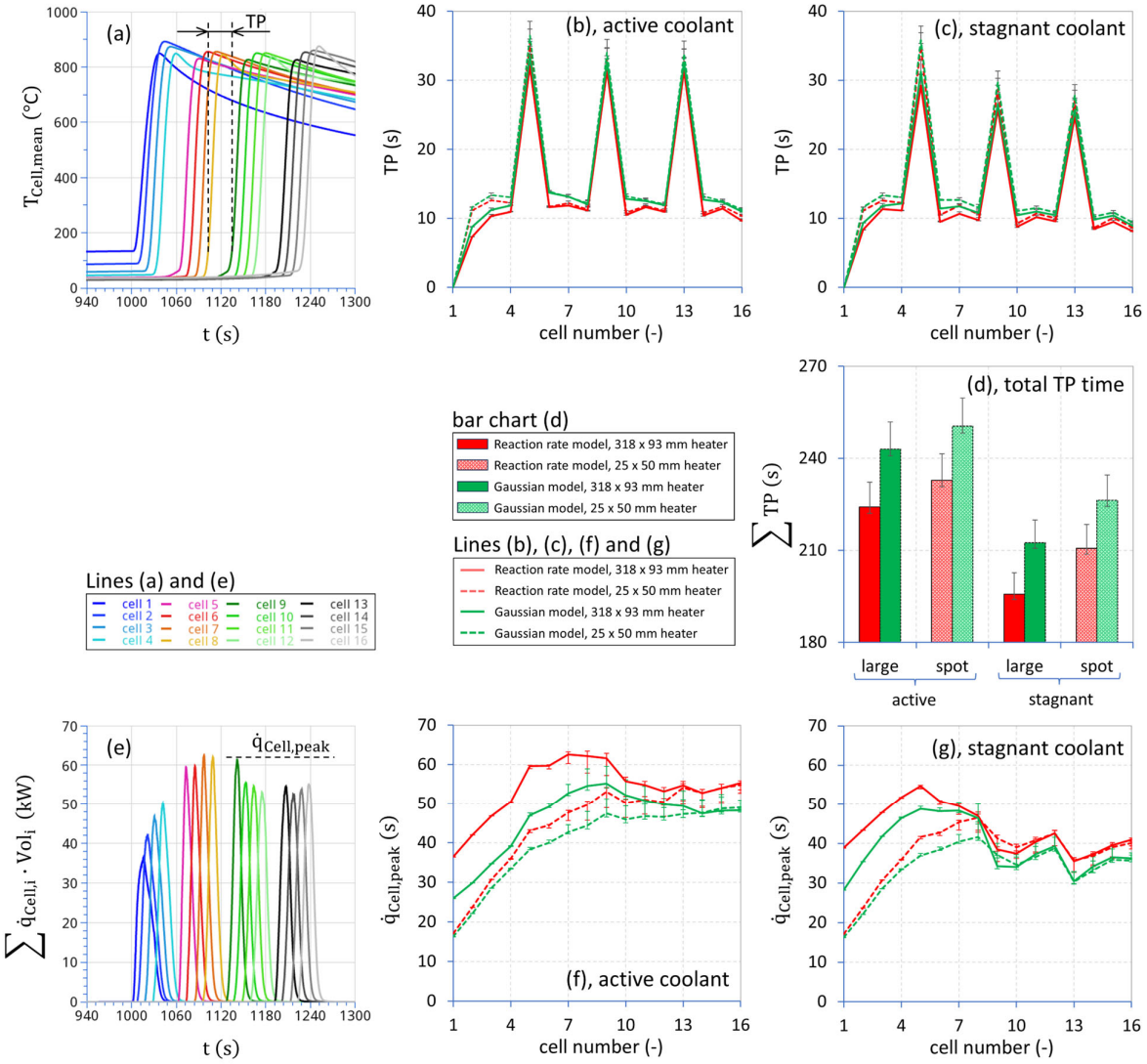

Figure 10. Two-dimensional summary from the 3D CFD simulation of the 4S4P battery module: (**a**) battery cell volumetric mean temperature for the reaction rate model under active coolant and 318 × 92 mm heater, (**b**) thermal propagation evaluated per Equation (36) for active coolant, (**c**) thermal propagation evaluated per Equation (36) for stagnant coolant, (**d**) thermal propagation accumulated from cell 1-18, (**e**) battery cell heat release for the reaction rate model under active coolant and 318 × 92 mm heater, (**f**) peak of battery cell heat release for active coolant, (**g**) peak of battery cell heat release for stagnant coolant.

Figure 10e–g illustrate the heat release intensity during thermal runaway and thermal propagation for both the reaction rate and the Gaussian models. To consistently compare all

models, cooling conditions, and trigger methods, the cell-wise peak heat release is defined as follows:

$$\dot{q}_{Cell,peak}(t) = \max\left(\sum_{i=1}^{N} \dot{q}_{Cell,i} \cdot Vol_i\right) \quad (37)$$

For the 25 × 50 mm heater, the $\dot{q}_{Cell,peak}$ of cells 1–7 is smaller than for the 318 × 92 mm heater. This is attributed to localized triggering. The smaller heater thermally activates a confined volume region. Due to thermal diffusion, the effective trigger area enlarges from cell to cell, such that from cell 8 onward, $\dot{q}_{Cell,peak}$ converges for both heater sizes.

Under active cooling, $\dot{q}_{Cell,peak}$ exceeds that of stagnant conditions. This is caused by enhanced convective heat diffusion. Heat released from already triggered cells is transported by the coolant to adjacent, not yet triggered cells. These cells, therefore, receive a broader-area heat input compared with stagnant conditions. Once activated, this leads to a more intense heat release accumulated across the entire battery volume.

4.4. Model Sensitivity on the Convective Heat Transfer Coefficient

As this study employs pre-defined convective boundary conditions, the sensitivity of both the ARC test model and the 4S4P battery CFD model to the convective heat transfer coefficient (HTC) is assessed. Simulations use an ambient temperature of 20 °C and a baseline HTC of 5 W/m^2K, representing free convection. A sensitivity range of 0–25 W/m^2K is examined to span adiabatic conditions (HTC = 0) up to enhanced convection.

For the ARC test CFD model, varying the HTC has only a mild influence on the results reported in Figures 5–7; both the local maximum and the volume-averaged temperature change by approximately ±0.6 °C. The cell heat release rate shown in Figure 3 varies by +0.6 kW/−1.8 kW over the tested HTC range.

Figure 10 summarizes the sensitivity for the 4S4P module. Thermal propagation accelerates under adiabatic conditions and slows for HTC > 5 W/m^2K. The propagation from cell 1 to cell 16 is up to 9.1 s slower at HTC = 25 W/m^2K compared with the baseline HTC = 5 W/m^2K. Peak cell-wise heat release during TR increases slightly under adiabatic conditions and decreases for HTC > 5 W/m^2K when using the Arrhenius reaction rate model. With stronger convection, slightly lower local peak temperatures reduce the Arrhenius source term and, consequently, the predicted heat release rate.

In contrast, the Gaussian model exhibits the opposite trend. Adiabatic conditions tend to reduce the peak heat release, while HTC > 5 W/m^2K increases it. This behavior arises from the model definition that truncates the source term at T_{max} = 850 °C (Figure 1). Under adiabatic conditions, local cell temperatures can peak at 850 °C, causing the Gaussian source term to vanish. As the temperature subsequently falls below 850 °C, heat release resumes. This on–off behavior repeats until the available reactant Y is consumed. The same mechanism influences the local peak cell temperature, as discussed in Section 4.2.

5. Conclusions

In this study, Arrhenius-type reaction rate modeling shows improved agreement between simulated and measured battery cell skin temperatures during thermal runaway for an NMC721 pouch cell. The model also tends to predict a slightly lower total thermal energy release and, in the case of a 4S4P battery module comprising NMC721 pouch cells, a 5–10% faster thermal propagation compared with Gaussian or polynomial TR models.

The discussed reaction rate model (Section 2.2.2) is based on a multi-stage concept, with each stage representing a distinct physical phase of the battery thermal runaway process. This concept is derived from characteristic features in the battery cell skin temperature evolution measured during an accelerated rate calorimetry (ARC) test of an NMC721 pouch cell. Decoupling the model stages enables the independent identification of the

corresponding reaction rate parameters (Section 2.3), thereby reducing parameter cross-correlation. This capability can provide a basis for parameterisation of more comprehensive thermal runaway models, including those discussed in Section 2.2.

Comparable thermal runaway characteristics have been reported by Golubkov et al. [7] for cylindric 18650 cells with LCO, NCA, and LFP cathodes, supporting the assumption that the proposed multi-stage reaction rate model may also be transferable to these chemistries. Across multiple chemistries and cell formats, Han et al. [9], Garcia et al. [10], Willstrand et al. [11], Essl et al. [12], Bugryniec et al. [13], Golubkov et al. [14], and Pfrang et al. [2] found a consistent trend of reduced T_{onset}, increased T_{max}, and increased temperature rates (dT/dt) with increasing SoC. Aged cells are found to exhibit earlier onset of thermal runaway and reduced exothermic heat release than fresh cells at identical SoC (see Section 2.3). Further, studies such as Essl et al. [15] on cell format effects indicate that in setups where a thermal resistance exists between the thermocouple and the battery's active material (e.g., cylindrical and prismatic hard case cells), reaction rate parameters must be calibrated to the setup rather than inferred directly from skin temperature measurements.

Thus, while the model structure appears transferable across cell formats and chemistries, the parameterization seems intrinsically tied to the specific test conditions, limiting predictive capability to cases with prior parameter identification from experimental data. To address model limitations connected to SoC and SoH, one could employ more general models capable of capturing both heat generation and electrochemical discharge behavior, as proposed by Coman et al. [19], Ostanek et al. [5], Xinyu et al. [36], and Garcia et al. [10]. An alternative potential future direction is to explore recently emerged data-driven methods. Shi et al. [37] showed that transfer learning models can predict exothermic heat release during thermal runaway and its cell-to-cell variability without extensive calorimetry, using metadata and mass-ejection measurements from cylindrical cells. A critical yet currently unaddressed parameter in their framework is the onset temperature of TR. Similarly, Zhang et al. [38] predict battery cycle life from deep learning (CNN) with intra- and inter-cell learning trained on data from multiple public datasets, enabling accurate cycle life prediction from only the first 20–100 cycles and reducing reliance on long cycling campaigns. While the targets differ (lifetime vs. heat release in TR), both frameworks demonstrate that data-driven learning across cells/conditions can reduce or replace traditional test campaigns. The integration of such extended modeling approaches, however, lies beyond the scope of the present work.

The conclusions contained in this report are those of the authors and should not be interpreted as an official policy or endorsement of AVL List GmbH, either expressed or implied.

Author Contributions: Conceptualization, A.R.; methodology, A.R.; software, A.R. and M.H.; validation, A.R. and M.H.; formal analysis, A.R.; investigation, A.R. and M.H.; resources, A.M. and A.E.; data curation, A.R.; writing—original draft, A.R. and M.H.; writing—review and editing, A.R., M.H., A.M., and A.E.; visualization, A.R. and M.H.; supervision, A.M. and A.E.; project administration, A.M.; funding acquisition, A.M. and A.E. All authors have read and agreed to the published version of the manuscript.

Funding: This research received no external funding from funding agencies in the public, commercial, or not-for-profit sectors.

Data Availability Statement: The data presented in this study are available upon request from the corresponding author. The data are not publicly available due to confidentiality.

Acknowledgments: This work was carried out at AVL List GmbH in Graz, Austria. The authors would like to thank all AVL colleagues for their useful discussions and support.

Conflicts of Interest: All authors were employed by the company AVL List GmbH. All authors declare that the research was conducted in the absence of any commercial or financial relationships that could be construed as a potential conflict of interest.

Abbreviations

The following abbreviations are used in this manuscript:

TR	Thermal Runaway	[–]
TP	Thermal Propagation	[–]
Li-ion	Lithium-Ion Battery	[–]
ARC	Accelerating Rate Calorimetry	[–]
DSC	Differential Scanning Calorimeter	[–]
SEI	Solid Electrolyte Interphase	[–]
ISC	Internal Short Circuit	[–]
3D	Three Dimensional	[–]
CFD	Computational Fluid Dynamics	[–]
CHT	Conjugate Heat Transfer	[–]
FV	Finite Volume	[–]
C	Battery Cell Electric Capacity	[Ah]
U	Battery Cell Open Circuit Voltage	[V]
$\dot{R}$	Reaction Rate	[1/s]
cp	Specific Heat	[J/kgK]
ρ	Density	[kg/m^3]
λ	Thermal Conductivity	[W/mK]
t	Time	[s]
x	x-Coordinate of Space	[m]
y	y-Coordinate of Space	[m]
z	z-Coordinate of Space	[m]
T	Temperature	[m]
A	Pre-Exponential Factor of Reaction Rate	[1/s]
E_a	Activation Energy of Reaction	[J/kg]
ΔH	Heat of Reaction	[J/g]
w	Specific Material Concentration	[g/m^3]
Y	Specific Amount of Reactant	[–]
$\dot{q}$	Current Heat Release	[W/m^3]
Q	Battery Total Thermal Energy	[J]
E	Battery Electric Energy	[J]
η	Proportionality of E and Q	[–]
m	Mass	[kg]
slope	Slope of Temperature Rate	[K^2/s]
b	Intercept	[–]
Vol	Total Volume of Battery Active Material	[m^3]
BC	Boundary Condition	[–]
R_u	Universal Gas Constant	[J/molK]
R^2	Pearson Correlation Coefficient	[–]

The following indices are used in this manuscript:

i	Indexing of finite volumes
N	Total number of finite volumes
j	Indexing of chemical reactions
j	Indexing for running averaging
M	Total number of chemical reactions

k	Index for thermocouple
k	Running average trailing window size
m	Index for thermal runaway model stage
n	Time index
Cell	Battery cell active material
before	Cell state before ARC test
after	Cell state after ARC test
onset	Time when thermal runaway is triggered
End	End of ARC test
TC	Thermocouple temperature
mean	Arithmetic mean value
max	Absolute maximum of evaluated data
min	Absolute minimum of evaluated data
ad	Adiabatic condition
Vent	Heat coming from vent gas
Particle	Heat coming from emitted particles
total	Total heat released from battery

References

1. Warner, J.T. Chapter 3—Lithium-ion battery operation. In *Lithium-Ion Battery Chemistries*; Elsevier Inc.: Amsterdam, The Netherlands, 2019; pp. 43–77.
2. Pfrang, A.; Kriston, A.; Ruiz, V.; Lebedeva, N.; di Persio, F. Chapter Eight—Safety of Rechargeable Energy Storage Systems with a focus on Li-ion Technology. In *Emerging Nanotechnologies in Rechargeable Energy Storage Systems*; Elsevier Inc.: Amsterdam, The Netherlands, 2017; pp. 253–290.
3. Liu, K.; Liu, Y.; Lin, D.; Pei, A.; Cui, Y. Materials for lithium-ion battery safety. *Sci. Adv.* **2018**, *4*, eaas9820. [CrossRef]
4. Citarella, M.; Suzzi, D.; Brunnsteiner, B.; Schiffbänker, P.; Maier, G.; Schneider, J. Computational Modelling of Thermal Runaway Propagation in Lithium-Ion Battery Systems. In Proceedings of the 2019 IEEE Transportation Electrification Conference (ITEC-India), Bengaluru, India, 17–19 December 2019.
5. Ostanek, J.K.; Li, W.; Mukherjee, P.P.; Crompton, K.R.; Hacker, C. Simulating onset and evolution of thermal runaway in Li-ion cells using a coupled thermal and venting model. *Appl. Energy* **2020**, *268*, 114972. [CrossRef]
6. Menz, F.; Bauer, M.; Böse, O.; Pausch, M.; Danzer, M.A. Investigating the Thermal Runaway Behaviour of Fresh and Aged Large Prismatic Lithium-Ion Cells in Overtemperature Experiments. *Batteries* **2023**, *9*, 159. [CrossRef]
7. Golubkov, A.W.; Fuchs, D.; Wagner, J.; Wiltsche, H.; Stangl, C.; Fauler, G.; Voitic, G.; Thaler, A.; Hacker, V. Thermal-runaway experiments on consumer Li-ion batteries with metal-oxide and olivin-type cathodes. *RSC Adv.* **2013**, *4*, 3633–3642. [CrossRef]
8. Li, Y.; Lu, Y.; Chen, L.; Hu, Y.-S. Failure analysis with a focus on thermal aspect towards developing safer Na-ion batteries. *Chin. Phys. B* **2020**, *29*, 048201. [CrossRef]
9. Han, Z.; Zhao, L.; Zhao, J.; Xu, G.; Liu, H.; Chen, M. An Experimental Study on the Thermal Runaway Propagation of Cycling Aged Lithium-Ion Battery Modules. *Fire* **2024**, *7*, 119. [CrossRef]
10. García, A.; Pastor, J.V.; Monsalve-Serrano, J.; Golke, D. Cell-to-cell dispersion impact on zero-dimensional models for predicting thermal runaway parameters of NCA and NMC811. *Appl. Energy* **2024**, *369*, 123571. [CrossRef]
11. Willstrand, O.; Pushp, M.; Andersson, P.; Brandell, D. Impact of different Li-ion cell test conditions on thermal runaway characteristics and gas release measurements. *J. Energy Storage* **2023**, *68*, 107785. [CrossRef]
12. Essl, C.; Golubkov, A.W.; Gasser, E.; Nachtnebel, M.; Zankel, A.; Ewert, E.; Fuchs, A. Comprehensive Hazard Analysis of Failing Automotive Lithium-Ion Batteries in Overtemperature Experiments. *Batteries* **2020**, *6*, 30. [CrossRef]
13. Bugryniec, P.J.; Davidson, J.N.; Cumming, D.J.; Brown, S.F. Pursuing safer batteries: Thermal abuse of $LiFePO_4$ cells. *J. Power Sources* **2019**, *414*, 557–568. [CrossRef]
14. Golubkov, A.W.; Scheikl, S.; Planteu, R.; Voitic, G.; Wiltsche, H.; Stangl, C.; Fauler, G.; Thaler, A.; Hacker, V. Thermal runaway of commercial 18650 Li-ion batteries with LFP and NCA cathodes—Impact of state of charge and overcharge. *RSC Adv.* **2015**, *5*, 57171–57186. [CrossRef]
15. Essl, C.; Golubkov, A.W.; Fuchs, A. Comparing Different Thermal Runaway Triggers for Two Automotive Lithium-Ion Battery Cell Types. *J. Electrochem. Soc.* **2020**, *167*, 130542. [CrossRef]
16. Yeow, K.F.; Teng, H. Characterizing Thermal runaway of lithium-ion cells in a battery system using finite element analysis approach. *SAE Int. J. Altern. Powertrains* **2013**, *2*, 179–186. [CrossRef]

17. Hatchard, T.D.; MacNeil, D.D.; Basu, A.; Dahn, J.R. Thermal Model of Cylindrical and Prismatic Lithium-Ion Cells. *J. Electrochem. Soc.* **2001**, *7*, 148. [CrossRef]
18. Kim, G.-H.; Pesaran, A.; Spotnitz, R. A three-dimensional thermal abuse model for lithium-ion cells. *J. Power Sources* **2007**, *170*, 476–489. [CrossRef]
19. Coman, P.T.; Darcy, E.C.; Veje, C.T.; White, R.E. Modelling Li-Ion Cell Thermal Runaway Triggered by an Internal Short Circuit Device Using an Efficiency Factor and Arrhenius Formulations. *J. Electrochem. Soc.* **2017**, *164*, A587–A593. [CrossRef]
20. Ostanek, J.; Parhizi, M.; Jeevarajan, J. A novel method for alleviating numerical stiffness in Li-ion thermal abuse models. *J. Power Sources Adv.* **2023**, *23*, 100123. [CrossRef]
21. Ostanek, J.K.; Parhizi, M.; Li, W.; Kilaz, G.; Crompton, K.R. CFD-Based Thermal Abuse Simulation including Gas Generation and Venting of an 18650 Li-Ion Battery Cell. *J. Electrochem. Scociety* **2023**, *170*, 090512. [CrossRef]
22. Parhizi, M.; Jain, A.; Kilaz, G.; Ostanek, J.K. Accelerating the numerical solution of thermal runaway in Li-ion batteries. *J. Power Sources* **2022**, *538*, 231531. [CrossRef]
23. Sorensen, A.; Utgikar, V.; Belt, J. A Study of Thermal Runaway Mechanisms in Lithium-Ion Batteries and Predictive Numerical Modeling Techniques. *Batteries* **2024**, *10*, 116. [CrossRef]
24. Sun, T.; Wang, L.; Ren, D.; Shi, Z.; Chen, J.; Zheng, Y.; Feng, X.; Han, X.; Lu, L.; Wang, L.; et al. Thermal Runaway Characteristics and Modeling of $LiFePO_4$ Power Battery for Electric Vehicles. *Automot. Innov.* **2023**, *6*, 414–424. [CrossRef]
25. MacNeil, D.D.; Dahn, J.R. Test of Reaction Kinetics Using Both Differential Scanning and Accelerating Rate Calorimetries as Applied to the Reaction of Li_xCoO_2 in Non-aqueous Electrolyte. *J. Phys. Chem. A* **2001**, *105*, 4430–4439. [CrossRef]
26. Peng, P.; Jiang, F. Thermal safety of lithium-ion batteries with various cathode materials: A numerical study. *Int. J. Heat Mass Transf.* **2016**, *103*, 1008–1016. [CrossRef]
27. Abada, S.; Petit, M.; Lecocq, A.; Marlair, G.; Sauvant-Moynot, V.; Huet, F. Combined experimental and modeling approaches of the thermal runaway of fresh and aged lithium-ion batteries. *J. Power Sources* **2018**, *399*, 264–273. [CrossRef]
28. Kim, J.; Mallarapu, A.; Finegan, D.P.; Santhanagopalan, S. Modelling Cell Venting and Gas-Phase Reactions In 18650 Lithium Ion Batteries During Thermal Runaway. *J. Power Sources* **2020**, *489*, 229496. [CrossRef]
29. Shelkea, A.V.; Buston, J.E.; Gill, J.; Howard, D.; Williams, R.C.; Read, E.; Abaza, A.; Cooper, B.; Richards, P.; Wen, J.X. Combined numerical and experimental studies of 21700 lithium-ion battery thermal runaway induced by different thermal abuse. *Int. J. Heat Mass Transf.* **2022**, *194*, 123099. [CrossRef]
30. Hoelle, S.; Scharner, S.; Asanin, S.; Hinrichsen, O. Analysis on Thermal Runaway Behavior of Prismatic Lithium-Ion Batteries with Autoclave Calorimetry. *J. Electrochem. Soc.* **2021**, *168*, 120515. [CrossRef]
31. Hoelle, S.; Zimmermann, S.; Hinrichsen, O. 3D Thermal Simulation of Thermal Runaway Propagation in Lithium-Ion Battery Cell Stack: Review and Comparison of Modeling Approaches. *J. Electrochem. Soc.* **2023**, *170*, 060516. [CrossRef]
32. Verein Deutscher Ingenieure [Hrsg.]. *VDI-Wärmeatlas*; Springer Vieweg: Berlin/Heidelberg, Germany, 2019.
33. Koller, M.; Unterkofler, J.; Glanz, G.; Lager, D.; Bergmann, A.; Popp, H. Radial Thermal Conductivity Measurements of Cylindrical Lithium-Ion Batteries—An Uncertainty Study of the Pipe Method. *Batteries* **2022**, *8*, 16. [CrossRef]
34. Feng, X.; He, X.; Ouyang, M.; Lu, L.; Wu, P.; Kulp, C.; Prasser, S. Thermal runaway propagation model for designing a safer battery pack with 25 Ah LiNi Co Mn O_2 large format lithium ion battery. *Appl. Energy* **2015**, *154*, 74–91. [CrossRef]
35. Feng, X.; Lu, L.; Ouyang, M.; Li, J.; He, X. A 3D thermal runaway propagation model for a large format lithium ion battery module. *Energy* **2016**, *115*, 194–208. [CrossRef]
36. Liu, X.; Zhou, Z.; Wu, W.; Gao, L.; Li, Y.; Huang, H.; Huang, Z.; Li, Y.; Song, Y. Three-Dimensional Modeling for the Internal Shorting Caused Thermal Runaway Process in 20Ah Lithium-Ion Battery. *Energies* **2022**, *15*, 6868. [CrossRef]
37. Shi, C.; Zhu, D.; Zhang, L.; Song, S.; Sheldon, B.W. Transfer learning prediction on lithium-ion battery heat release under thermal runaway condition. *Nano Res. Energy* **2024**, *3*, e9120147. [CrossRef]
38. Zhang, H.; Li, Y.; Zheng, S.; Lu, Z.; Gui, X.; Xu, W.; Bian, J. Battery lifetime prediction across diverse ageing conditions with inter-cell deep learning. *Nat. Mach. Intell.* **2023**, *7*, 270–277. [CrossRef]